Thermal and Manufacturing Design Considerations for Silicon-Based Embedded Microchannel-3D Manifold Coolers (EMMCs): Part 1—Experimental Study of Single-Phase Cooling Performance With R-245fa

Ki Wook Jung
Department of Mechanical Engineering,
Stanford University,
Stanford, CA 94305

Eunho Cho
School of Mechanical Engineering,
Chung-Ang University,
Seoul 06974, South Korea

Hyoungsoon Lee
School of Mechanical Engineering,
Chung-Ang University,
Seoul 06974, South Korea

Chirag Kharangate
Department of Mechanical and
Aerospace Engineering,
Case Western Reserve University,
Cleveland, OH 44106

Feng Zhou
Toyota Research Institute of North America,
Ann Arbor, MI 48105

Mehdi Asheghi
Department of Mechanical Engineering,
Stanford University,
Stanford, CA 94305

Ercan M. Dede
Toyota Research Institute of North America,
Ann Arbor, MI 48105

Kenneth E. Goodson[1]
Department of Mechanical Engineering,
Stanford University,
Stanford, CA 94305
e-mail: goodson@stanford.edu

High performance and economically viable cooling solutions must be developed to reduce weight and volume, allowing for a wide-spread utilization of hybrid electric vehicles. The traditional embedded microchannel cooling heat sinks suffer from high pressure drop due to small channel dimensions and long flow paths in two-dimensional (2D) plane. Utilizing direct "embedded cooling" strategy in combination with top access three-dimensional (3D) manifold strategy reduces the pressure drop by nearly an order of magnitude. In addition, it provides more temperature uniformity across large area chips and it is less prone to flow instability in two-phase boiling heat transfer. This study presents the experimental results for single-phase thermofluidic performance of an embedded silicon microchannel cold plate (CP) bonded to a 3D manifold for heat fluxes up to 300 W/cm^2 using single-phase R-245fa. The heat exchanger consists of a 5×5 mm^2 heated area with 25 parallel 75×150 μm^2 microchannels, where the fluid is distributed by a 3D-manifold with four microconduits of 700×250 μm^2. Heat is applied to the silicon heat sink using electrical Joule-heating in a metal serpentine bridge and the heated surface temperature is monitored in real-time by infrared (IR) camera and electrical resistance thermometry. The maximum and average temperatures of the chip, pressure drop, thermal resistance, and average heat transfer coefficient (HTC) are reported for flow rates of 0.1, 0.2. 0.3, and 0.37 L/min and heat fluxes from 25 to 300 W/cm^2. The proposed embedded microchannels-3D manifold cooler, or EMMC, device is capable of removing 300 W/cm^2 at maximum temperature 80 °C with pressure drop of less than 30 kPa, where the flow rate, inlet temperature, and pressures are 0.37 L/min, 25 °C and 350 kPa, respectively. The experimental uncertainties of the test results are estimated, and the uncertainties are the highest for heat fluxes < 50 W/cm^2 due to difficulty in precisely measuring the fluid temperature at the inlet and outlet of the microcooler. [DOI: 10.1115/1.4047846]

Keywords: embedded microchannels, 3D-manifold, single-phase R-245fa, infrared (IR) measurement

1 Introduction

Effective liquid thermal management solutions are required as the power densities for modern power electronics have increased considerably over the past decades. Tuckerman and Pease [1] reported a microscale, straight channel heat exchanger that could remove ~800 W/cm^2 with hydraulic diameter of ~90 μm; however, there were excessive pressure drop, ranging from 100 to 215 kPa.

A combination of microchannels with three-dimensional (3D) manifold routing (vertical liquid delivery and distribution scheme) has been proposed to overcome the large pressure drop in conventional lateral liquid feeding approach [2–9]. This approach is preferred because the smaller hydraulic diameter yields improved thermal performance; however, the out-of-plane liquid delivery to each channel results in shorter paths for liquid, thus reducing the pressure drop compared to the conventional microchannel heat exchangers. Drummond et al. [2,3] developed and tested a microchannel heat exchanger with multilayer hierarchical manifolds using R-245fa that removed heat flux up to ~1 kW/cm^2 with thermal resistance of 0.07 cm^2-K/W, and pressure drop from 50 to 120 kPa [3] for two-phase heat transfer. Cetegen [4] also utilized a similar heat exchanger architecture, called forced-fed microchannel heat sink (FFMHS), using R-245fa as the working fluid. The cooling performance of the optimized FFMHS was 72% and 306% more effective than traditional microchannel heat sinks, and jet impingement heat sinks, respectively. The maximum heat flux

[1]Corresponding author.

Contributed by the Electronic and Photonic Packaging Division of ASME for publication in the Journal of Electronic Packaging. Manuscript received January 16, 2020; final manuscript received April 11, 2020; published online August 17, 2020. Assoc. Editor: Sukwon Choi.

removable from the module was ~1.2 kW/cm^2 with the thermal resistance of 0.06 cm^2-K/W. The reported pressure drop ranged from a few kPas to 60 kPa for two-phase cooling. Cooligy, a Stanford Startup Company developed and commercialized a heat sink that uniformly distributes the working fluid to normal direction of a microfluidic heat exchange part [5]. The design of the microfluidic heat exchange part is flexible by having either microchannels, micropin-fins, or microporous foams [6]. Zhou et al. [8] from Toyota Research Institute of North America tested two chip-scale cooling devices, a straight microchannel cooler and a unit cell microchannel with jet impingement cooler, in single-phase water. The unit cell microchannel device removed the maximum heat flux of 1.02 kW/cm^2 with a measured pressure drop of 41.2 kPa, which showed superior thermal-fluidic performance to the straight microchannel device [10].

This paper, the first of trilogy published at the ASME *Journal of Electronic Packaging*, reports an experimental investigation of cooling performance in an embedded microchannel-3D manifold cooler (EMMC), using single-phase R-245fa. The second paper provides a parametric study of cooling performance of the EMMCs using computational fluid dynamics (CFD) modeling [11], and the last volume addresses the manufacturing challenges using laser ablation process [12].

In this study, four different flow rates are tested from 0.1 to 0.37 L/min with the inlet fluid temperature of 25 °C and heat fluxes up to 300 W/cm^2. The parameters of interest to describe the thermofluidic performance are heated surface temperature, inlet/outlet fluid temperatures, thermal resistances, heat transfer coefficients (HTCs) at the cold-plate (CP) microchannel walls, and pressure drops. In Sec. 4, and Appendices A2 and A3, these parameters are carefully described, then experimental data and uncertainties are reported. The temperature distribution over the 5 mm × 5 mm heated area is measured using a high spatial resolution infrared (IR) camera, the maximum and average temperatures are reported. The experimental uncertainties of the test results are calculated, and the uncertainties are the highest for heat fluxes <50 W/cm^2 due to difficulty in precisely measuring the fluid temperature at the inlet and outlet of the microcooler.

2 Experimental Method

2.1 Design of Embedded Microchannel-3D Manifold Cooler. The EMMC consists of two parts: a CP and a fluid manifold substrate. Anisotropically etched microchannels are defined on one side of the CP, and a serpentine Au/Ti heater is deposited on the other side of the CP. Likewise, inlet openings, inlet plenums, and inlet/outlet conduits are anisotropically etched into the manifold substrate from both sides.

Figure 1(*a*) describes the working principle of the EMMC. The fluid is supplied through the fluid inlet openings (1) from the backside of the manifold substrate and it is uniformly distributed within the inlet plenums (2). The distributed fluid passes the gradual contraction region (between 2 and 3) and keeps flowing through the inlet conduits (3) until it reaches to the intersections between the manifold inlet conduits and the CP microchannels (between 3 and 4). At the intersection, the fluid is diverged and the partial fluid moves toward the CP microchannels' heated section by making a 90 deg-turn. The diverged fluid proceeds along the CP microchannels and heat is transferred from the CP

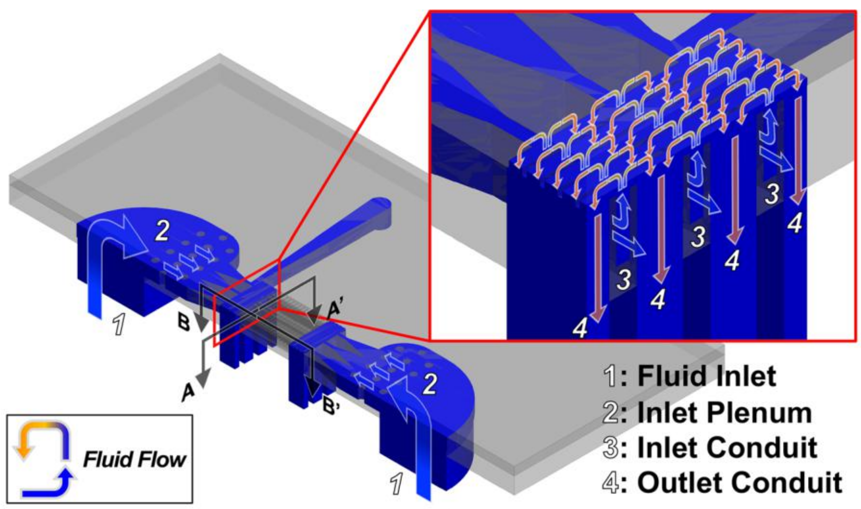

(*a*)

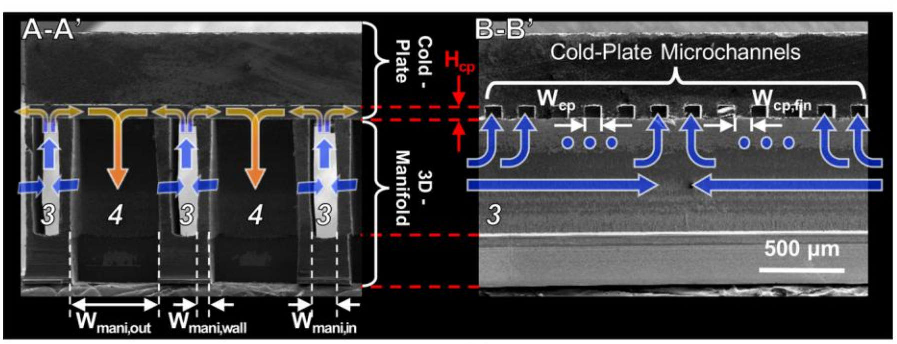

(*b*)

Fig. 1 Conceptual design of an embedded microchannel-3D manifold (EMMC); (*a*) representation of the fluid flow pattern inside the EMMC and (*b*) a SEM image of cross-sectional view of the actual EMMC device

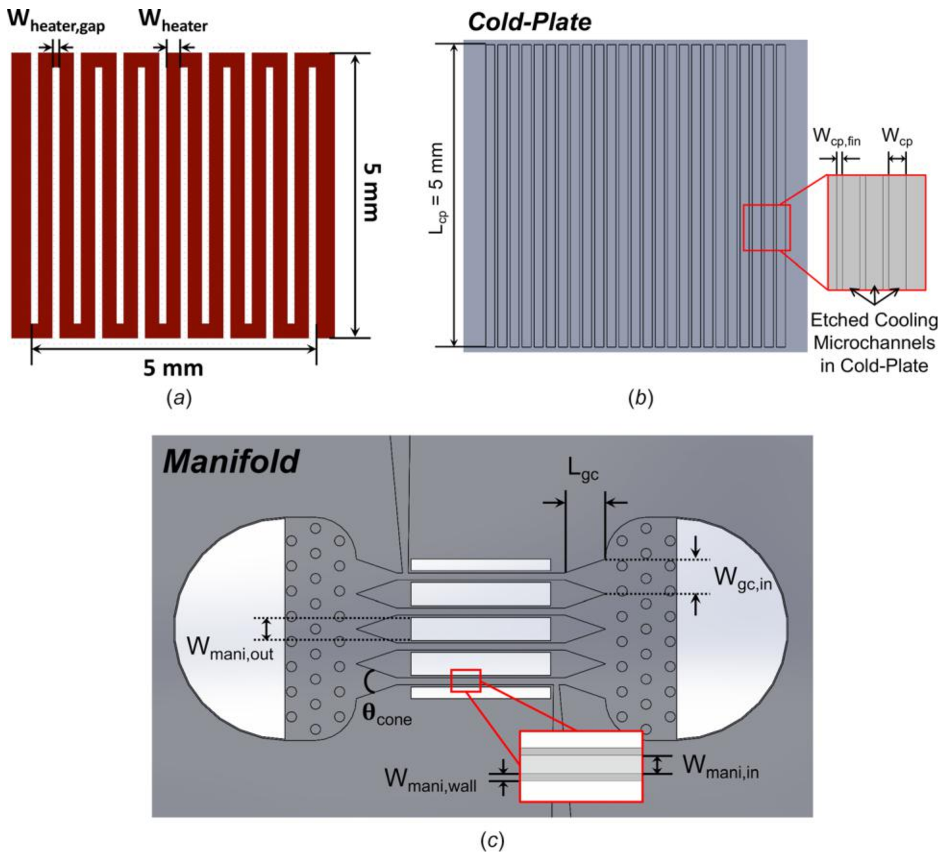

Fig. 2 Geometric parameters of microfeatures in (*a*) serpentine heater, (*b*) cold plate, and (*c*) 3D-manifold

microchannels' surface to the fluid until it exits through the adjacent manifold outlet conduits (4) by making another 90 deg turn. The nondiverged fluid at the intersection keeps flowing along the manifold inlet conduits until it reaches to the next intersection and the same flow pattern as described earlier is repeated. Figure 1(*b*) is SEM images of a fabricated test sample that show the placement of CP microchannel, manifold inlet/outlet conduits and depicts how the 90 deg-turns are made inside of the device with 3D arrows.

Important geometric parameters are introduced in Fig. 2. The key dimensions to describe the geometry of a Ti/Au serpentine heater (20 and 500 nm of thickness, respectively), CP microchannels, and microstructures in the manifold are listed in Table 1.

Table 1 Dimensions of structures in the cold plate and the manifold

Substrate	Structures	Parameters	Dimensions
Cold plate	Microchannel	H_{cp}	75 μm
		W_{cp}	150 μm
		$W_{cp,fin}$	50 μm
	Serpentine heater	W_{heater}	250 μm
		$W_{heater,gap}$	125 μm
Manifold	Inlet conduit	$H_{mani,in}$	700 μm
		$W_{mani,in}$	250 μm
		$W_{mani,wall}$	85 μm
	Outlet conduit	$H_{mani,out}$	1000 μm
		$W_{mani,out}$	830 μm
	Inlet plenum	$W_{gc,in}$	1.24 mm
		L_{gc}	1.45 mm
		θ_{cone}	37.70 deg

2.2 Calibration of Infrared Measurement. A FLIR A-655sc IR camera is used to measure the heated surface temperature in real-time. The hotspot area is coated with black spray paint and the emissivity of the painted surface is determined by comparing the surface temperature measured by IR camera to the surface temperature measured by electrical resistance thermometry method.

Figure 3(*a*) shows the schematic of the IR measurement setup and calibration process. The fluid is heated up by the preheater installed before the test section, where the working fluid is pumped at high flow rates. The inlet and outlet fluid temperatures are measured by two calibrated K-type thermocouples, the average of the inlet and outlet temperatures, $T_{heater,avg}$, were used as reference point for IR thermometry calibration. The electrical resistance of the heater is also calibrated independently in an oven, and along with the average reference temperature (in agreement within 1 °C) are used to estimate the emissivity ($\sim$0.95) of the chip surface (see Fig. 3(*b*)). Figure 3(*c*) shows typical IR images for the maximum removable heat flux, 298 W/cm^2 at the flow rate of 0.37 L/min. In this paper, the average heater surface temperature is measured by both electrical resistance thermometry and compared with the average IR temperature.

3 Theoretical Analysis

3.1 Data Reduction. The metal serpentine heater is powered by Joule heating, q_{heater}, and it is calculated by multiplying the voltage drop across the heater, ΔV_{heater}, and the current flowing through the heater, I_{heater}

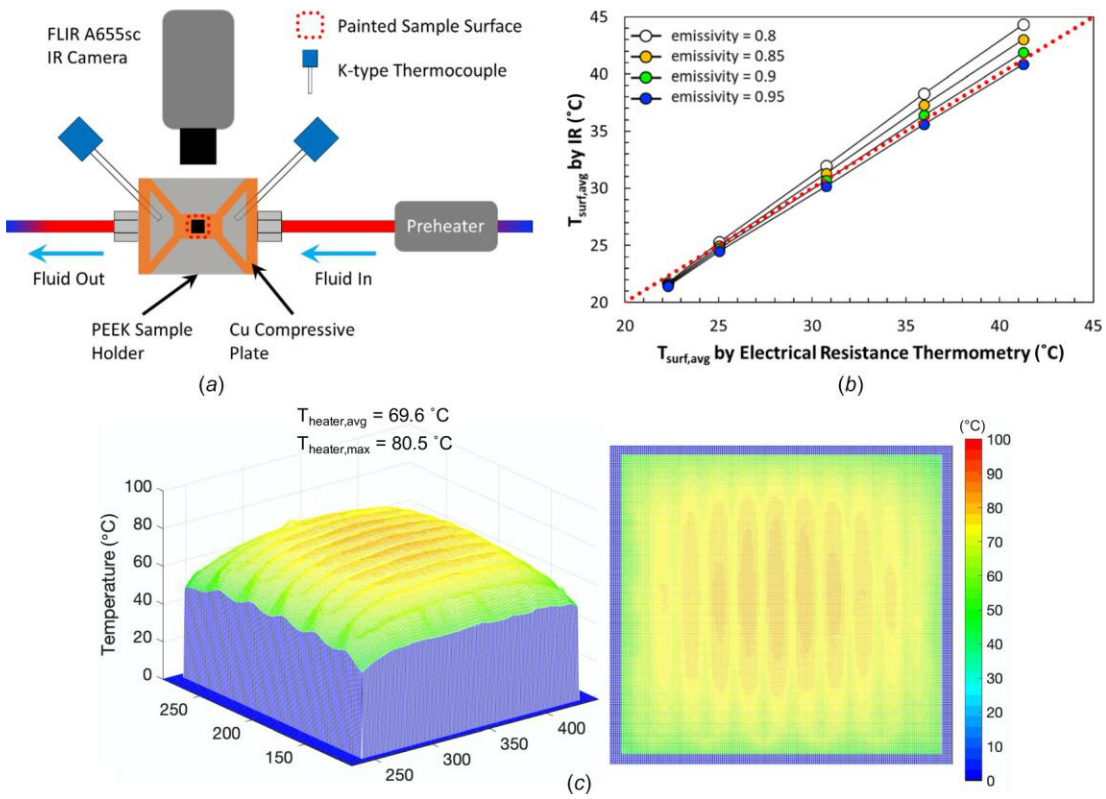

Fig. 3 Description of the IR calibration procedure: (*a*) conceptual image of the IR measurement setup, (*b*) determination of the emissivity of the black body, emissivity of 0.95 performs best among others, and (*c*) typical IR images showing surface temperature distribution of the heated surface from perspective and top views for 298 W/cm^2, single-phase R-245fa at flow rate of 0.37 L/min, the maximum and average heat temperatures are 80.5 °C and 69.5 °C, respectively

$$q_{\text{supply}} = \Delta V_{\text{heater}} \cdot I_{\text{heater}} \tag{1}$$

The supplied heat is transferred from the metal layer to the bulk Si, to the R-245fa dielectric working fluid. The net heat transferred to the fluid, q_{trans}, is estimated by observing the sensible heat change of the fluid

$$q_{\text{trans}} = q_{\text{supply}} - q_{\text{loss}} = \dot{m} \cdot \int_{T_{\text{f,in}}}^{T_{\text{f,out}}} C_p(T)\mathrm{d}T = \sum_{\text{i}=1}^{n} \mathrm{d}q_{\text{trans},i} \tag{2a}$$

$$\mathrm{d}q_{\text{trans,i}} = \dot{m} \cdot \frac{C_{\text{p,i}} + C_{\text{p,i+1}}}{2} \cdot \frac{T_{f,\text{out}} - T_{f,\text{in}}}{n}, \quad n = \frac{T_{\text{f,out}} - T_{\text{f,in}}}{\delta_T} \tag{2b}$$

where C_p is the saturated specific heat of single-phase R-245fa and it is temperature-dependent. If we define the finite interval of temperature, δ_{T}, as 0.1 °C, the number of intervals between $T_{f,\text{out}}$ and $T_{f,\text{in}}$, n, is determined and the finite q_{trans} at ith interval, $\mathrm{d}q_{\text{trans,i}}$, can be calculated. The numerical integration of $\mathrm{d}q_{\text{trans,i}}$ is the overall transmitted heat to the working fluid. Since the heater is made of pure metal layers, Ti and Au, the resistance of the heater, Z_{heater}, is linearly changed as the heater temperature is changed

$$T_{\text{heater,avg}} = T_0 + \frac{Z_{\text{heater}} - Z_0}{\alpha \cdot Z_0} \tag{3a}$$

$$Z_{\text{heater}} = \frac{\Delta V_{\text{heater}}}{I_{\text{heater}}} \tag{3b}$$

where T_0 is the room temperature, Z_0 is the heater resistance at the room temperature, and α is the temperature coefficient of resistance (TCR) of the heater.

The cooling performance of the EMMC can be described by the total thermal resistance, R_{total}, and it consists of multiple terms

$$R_{\text{total}} = R_{\text{cond}} + R_{\text{conv}} + R_{\text{adv}} = \frac{T_{\text{heater,avg}} - T_{\text{f,in}}}{q''_{\text{trans}}} \tag{4a}$$

$$R_{\text{cond}} = \frac{T_{\text{heater,avg}} - T_{\text{cp,base,avg}}}{q''_{\text{trans}}} \tag{4b}$$

$$R_{\text{conv}} = \frac{T_{\text{cp,base,avg}} - T_{\text{f,ref}}}{q''_{\text{trans}}} \tag{4c}$$

$$R_{\text{adv}} = \frac{T_{\text{f,ref}} - T_{\text{f,in}}}{q''_{\text{trans}}} \tag{4d}$$

where R_{cond} is the conduction thermal resistance in solid substrates, R_{conv} is the convection thermal resistance between the CP microchannel wall and the working fluid, and R_{adv} is the advection thermal resistance that indicates the increase in the average temperature of the fluid.

The HTC is defined as a convective heat transfer rate at the CP microchannel walls and it is expressed as

$$\text{HTC} = \frac{q_{\text{trans}}}{\eta_{\text{o}} \cdot (T_{\text{cp,base,avg}} - T_{\text{f,ref}}) \cdot A_{\text{wet}}} \tag{5}$$

where η_{o} is the overall fin efficiency, $T_{\text{cp,base,avg}}$ is the average temperature of the CP channel base that is calculated by conduction resistance across the metal/Si layers, $T_{\text{f,ref}}$ is the average fluid temperature between inlet and outlet, and A_{wet} is the wetted area of the CP microchannels

Table 2 Sources of measurement uncertainties for data analysis

Components	Affected parameters	Accuracy
Thermocouple (K-type)	T_0, $T_{\mathrm{f,in}}$, $T_{\mathrm{f,out}}$	$\pm 0.1\,^\circ$C
HP34401A multimeter	$\Delta V_{\mathrm{heater}}$, I_{heater}	$\pm 0.1\%$
Temperature coefficient of resistance, Au[a]	α	$\pm 0.1\%$
Micro motion CMFS010 Coriolis mass flow meter	Q_{total}	$\pm 0.10\%$ of rate (liquid)
Omega PX2300-5DI	$\Delta P_{\mathrm{total}}$	$\pm 0.25\%$ root sum square full scale (full scale: 0–5 psi)

[a]Temperature coefficient of resistance, or TCR, of Au is the material's property, but it can be differed by deposition conditions. The measured TCR of Au heater is 0.0033/° C, which is close to the reported TCR of Au bulk [13].

$$T_{\mathrm{cp,base,avg}} = T_{\mathrm{heater,avg}} - q''_{\mathrm{trans}} \cdot \sum_i \frac{\delta_i}{k_i} \tag{6a}$$

$$T_{\mathrm{f,ref}} = \frac{T_{\mathrm{f,in}} + T_{\mathrm{f,out}}}{2} \tag{6b}$$

$$\eta_{\mathrm{o}} = 1 - \frac{N_{\mathrm{cp}} \cdot A_{\mathrm{fin}}}{A_{\mathrm{wet}}} \cdot (1 - \eta_{\mathrm{fin}}) \tag{6c}$$

where N_{cp} is the number of CP microchannels and η_{fin} is the fin efficiency defined as

$$\eta_{\mathrm{fin}} = \frac{\tanh(m \cdot H_{\mathrm{cp}})}{m \cdot H_{\mathrm{cp}}}, \quad m = \sqrt{\frac{2 \cdot \mathrm{HTC}}{k_{\mathrm{Si}} \cdot W_{\mathrm{cp,fin}}}} \tag{6d}$$

The HTC is first calculated by assuming the fin efficiency of unity in Eq. (6c). After then, the fin efficiency is iterated until the HTC is converged. In this paper, the calculated η_{o} for all flow rates and heat fluxes is ~99%.

The total pressure drop in the EMMC, $\Delta P_{\mathrm{total}}$, is described as follows:

$$\Delta P_{\mathrm{total}} = \Delta P_1 + \Delta P_2 + \Delta P_3 + \Delta P_4 \cong \Delta P_2 + \Delta P_3 \tag{7}$$

where ΔP_1 is the pressure drop from the inlet openings to the inlet plenums, ΔP_2 is the pressure drop within the gradual contraction regions, from the end of the inlet plenums to the beginning of the active cooling region, ΔP_3 is the pressure drop where the convective heat transfer occurs, ΔP_4 is the expansion pressure drop after the fluid exits through the manifold outlet conduits. According to the CFD simulations by Jung et al. [7], the fluid across the manifold inlet conduits is uniformly distributed. In addition, it was concluded that the sum of ΔP_1 and ΔP_4 contributes to less than 5% of $\Delta P_{\mathrm{total}}$ based on conjugate CFD simulation results. A rough estimation of the ΔP_2 and ΔP_3 values is outlined in Appendix A2.

3.2 Uncertainty Study. Seven important parameters to investigate the thermofluidic performance of the EMMC are expressed by Eqs. (1)–(7). In order to estimate the uncertainties of these parameters, sources of measurement uncertainties are needed and they are listed in Table 2. The detailed expression of each parameter's uncertainty is described in Appendices A2 and A3.

4 Results and Discussion

4.1 Surface Temperature. Figure 4 describes the behavior of average heated surface temperature as the flow rate and the supplied heat are changed. The average surface temperatures, $T_{\mathrm{heater,avg}}$, versus total pressure drops, $\Delta P_{\mathrm{total}}$, for supplied heat fluxes, q_{heater}, from 25 to 300 W/cm^2 are depicted in Fig. 4(*a*). As expected, the average temperature increases with the increased q_{heater}, and decreases with the increased flow rates. In addition, the onset of nucleate boiling (ONB) is delayed as the flow rate increases. Figure 4(*b*) depicts the measured $T_{\mathrm{heater,max}}$, $T_{\mathrm{heater,avg}}$, $T_{\mathrm{f,out}}$ at a constant flow rate of 0.3 L/min, and they all increase linearly with the increase heat flux as expected for single-phase flow. The measured average temperature of the heater using IR and electrical resistance thermometry method agrees well with each other.

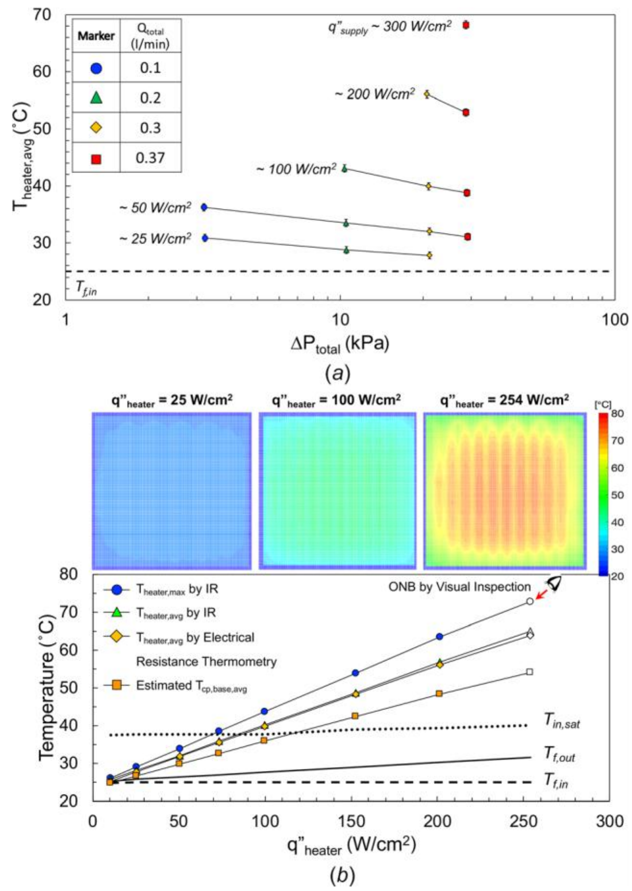

Fig. 4 Experimental results, (*a*) $T_{\mathrm{heater,avg}}$ versus $\Delta P_{\mathrm{total}}$, the supplied heat and the fluid flow rate are up to 300 W/cm^2 and 0.37 L/min, respectively and (*b*) measured temperatures versus supplied heat flux at a given flow rate of 0.3 L/min, open marker represents the ONB or two-phase regime (see Appendix A1 for details)

In addition, the inlet pressure is changing as the flow rate increases from 0.1 to 0.37 L/min; therefore, the saturated fluid temperature at the outlet (see Table 3) also increases due to a combination of the total pressure drop and the inlet pressure shift. In Appendix A1, we take the pressure shift into account for the analytic estimation of the ONB points.

4.2 Thermal Resistances. Figure 5 shows that for a given heat flux, the total thermal resistance, R_{total}, decreases with the increased flow rate. More specifically, both the convection and the

Table 3 Gradual increase in the saturated fluid outlet temperature

Flow rate (L/min)	Range of P_{in} (kPa)	Range of P_{out} (kPa)	Saturated fluid outlet temperature (°C)
0.1	219–224	216–221	35.9–36.6
0.2	235–241	225–230	38.1–38.7
0.3	254–267	233–247	40.4–41.9
0.37	332–358	303–329	48.8–51.2

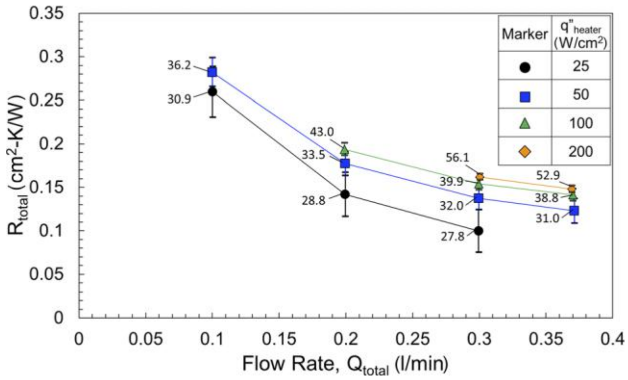

Fig. 5 Behavior of total thermal resistance as the flow rate changes and the supplied heat flux changes is presented by R_{total} versus Q_{total}. Numbers next to the markers are $T_{heater,avg}$.

advection thermal resistances, R_{conv}, R_{adv}, are decreasing because of the reduced microchannel base temperature, $T_{cp,base,avg}$, and the reduced fluid temperature, $T_{f,ref}$, respectively (Eqs. (4a)–4(d)). At higher flow rate, the rate of reduction in the total resistance R_{total} decreases since the $R_{conv} \sim Re^{-1/2}$, and as we approach the conduction resistance limit of $R_{cond} \sim 0.04\,cm^2$-K/W (due to 400 μm thick silicon substrate). Therefore, further reduction in R_{total} by increasing the flow rate higher than 0.37 L/min should not be expected.

The R_{total} at a given flow rate increases as the supplied heat flux increases, which is somewhat counterintuitive and unexpected. The uncertainty bars for the 25 W/cm^2 are large because the error associated with the temperature difference between the inlet fluid and average chip temperature (~3–5 °C). At higher heat fluxes 50–200 W/cm^2, the thermal resistance data are closer and small differences can be partially attributed to the temperature-dependent thermophysical properties of R-245fa. More details are presented and discussed in Fig. 6. In general, CFD modeling at low heat fluxes and high flow rates is recommended due to large uncertainty in the experimental results. There seems to be a systematic error in calculation of the net heat transferred to the fluid, q_{trans}, at low heat fluxes of 25–50 W/cm^2. For the microchannel with 3D-manifold, it is extremely hard to get access to the inlet and outlet plenums in order to insert thermocouples for measuring the inlet and outlet temperatures. As a result, the thermocouples are located at some distance away in the sample holder, and therefore susceptible to error associated with the heat loss from the fluid at the exit and heat gain at the entrance. Therefore, it is expected to see larger (and possibly systematic) error in calculation of q_{trans}, at the low heat fluxes. We have decided to share the thermal resistance results in order to demonstrate low fidelity results to be expected at low heat fluxes.

In Fig. 6, the total thermal resistance, R_{total}, and contributing components are plotted as a function of applied heat flux at the fixed flow rate of 0.3 L/min. As expected, R_{cond} and R_{adv} are nearly constant as the supplied heat flux increases. Such large increase in R_{conv} (and thus R_{total}) with heat flux is not expected but could be partially attributed to the temperature-dependent

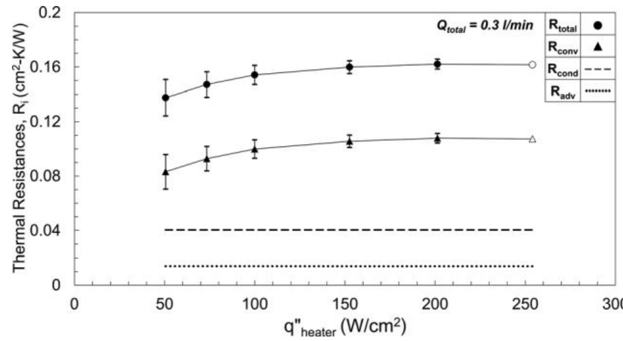

Fig. 6 Thermal resistances versus supplied heat flux at 0.3 L/min flow rates; open marker represents the ONB or two-phase regime

Table 4 Prandtl and Reynolds numbers, and thermal conductivity of R-245fa at given heat fluxes with 0.3 L/min flow rate

q''_{heater} (W/cm^2)	Pr	Re	kf (W/m-K)
51	6.00	739	0.0898
73	5.98	741	0.0897
100	5.97	743	0.0896
153	5.94	750	0.0894
201	5.91	756	0.0892

thermophysical properties of R-245fa, see Table 4. Both Pr and k_f decrease as the supplied heat flux increases; therefore, increasing trend in the thermal resistance would be expected but cannot explain the large variation in HTC between 50 and 250 W/cm^2. As we discussed, this is due to larger uncertainty in measurement of inlet and outlet fluid temperatures that are used in calculation of net heat transferred to fluid, q_{trans}.

The size of R_{total} and R_{conv} uncertainty bars decreases as the supplied heat flux increases because the main sources of R_{total} and R_{conv} uncertainties are $(U_{T_{heater,avg}}/q''_{trans})$, $(U_{T_{cp,base,avg}}/q''_{trans})$, respectively (refer to Eqs. (A11) and (A12) in Appendix A3); therefore, both of the uncertainties decrease as the q''_{trans} increases. Detailed description regarding the uncertainty calculation of the thermal resistances is discussed in Appendix A3.

4.3 Heat Transfer Coefficients. Heat transfer coefficients of the tested sample, HTCs, are estimated by Eq. (5), and plotted in Fig. 7. In Fig. 7, HTC increases with the increased Q_{total}. In single phase, HTC increases with the increased fluid flow rate. The uncertainty bars for the 25 W/cm^2 are large but at higher heat fluxes 50–200 W/cm^2, the HTC data are closer and small differences can be partially attributed to the temperature-dependent

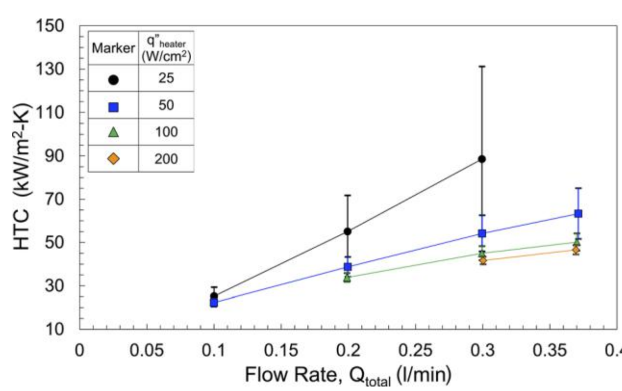

Fig. 7 The measured HTC at the cold-plate microchannel walls versus flow rate, the overall fin efficiency is from 98.4 to 99.4%

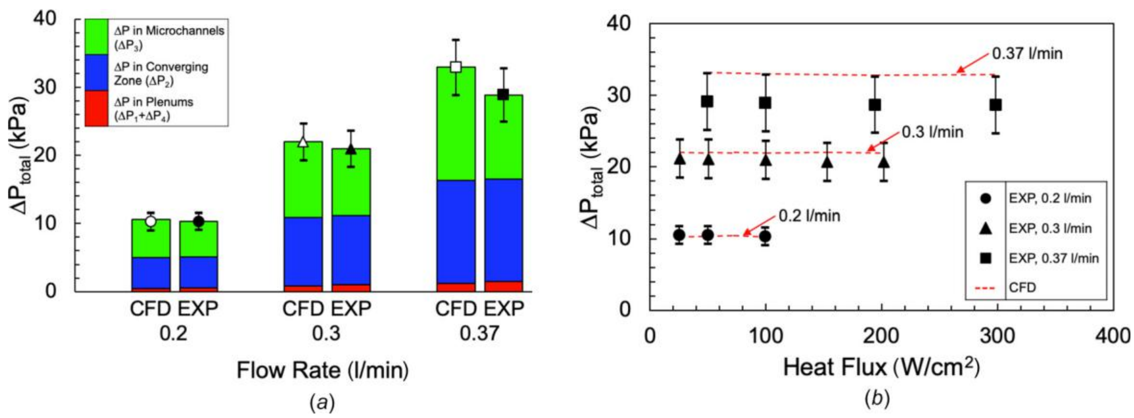

Fig. 8 Pressure drop results from the experiments are compared with the conjugate CFD simulation results. The total pressure drops from the CFD simulations are within the error of the total pressure drops from the experiments. (*a*) Pressure drops versus flow rate at a constant heat flux of 100 W/cm^2. (*b*) The total pressure drop results are plotted as a function of supplied heat flux. Since the tested fluidic flow is single-phase, change in the total pressure drop is less than 4%.

Table 5 Rough estimation of fluid velocities and Reynolds numbers within the gradual contraction region at the constant heat flux of 100 W/cm^2

Flow rate (L/min)	$v1$ (m/s)	$v2$ (m/s)	Re1	Re2	$\Delta P_{2,\text{est}}$ (kPa)	$\Delta P_{3,\text{est}}$ (kPa)
0.2	4.78×10^{-1}	2.37×10	1.41×10^3	2.88×10^3	4.60×10	5.25×10
0.3	7.19×10^{-1}	3.57×10	2.13×10^3	4.34×10^3	1.01×10^1	9.84×10
0.37	8.88×10^{-1}	4.41×10	2.63×10^3	5.36×10^3	1.51×10^1	1.24×10^1

thermophysical properties of R-245fa. The size of the HTC uncertainty, U_{HTC}, increases with the increased fluid flow rate, Q_{total}, at constant q''_{heater} because the temperature difference between the microchannel base, $T_{\text{cp,base,avg}}$, and the average fluid temperature, $T_{\text{f,ref}}$, decreases with the increased Q_{total} (refer to Eq. (A13) in Appendix A3).

4.4 System Pressure Drop. Some general descriptions regarding the changing trends of the pressure drop can be stated as:

(i) The total pressure drop increases with the increased flow rate,
(ii) the total pressure drop decreases as the supplied heat flux increases because the dynamic viscosity of the coolant decreases with the increased fluid temperature.

In Fig. 8(*a*), the resulting plot shows that the change in ΔP_{total}, $\Delta P_{2,\text{est}}$, and $\Delta P_{3,\text{est}}$ at a supplied heat flux of 100 W/cm^2. The experimental pressure drop results are compared with the CFD simulation results. As we discussed in the Sec. 3.1 part, ΔP_1 and ΔP_4 are less than 5% of ΔP_{total} and the estimation of ΔP_2 and ΔP_3, $\Delta P_{2,\text{est}}$, and $\Delta P_{3,\text{est}}$, respectively, can be obtained using the Bernoulli equation with kinetic energy correction factors (see Eqs. (A1)–(A3) in Appendix A2). By checking ΔP_2 and ΔP_3 values from the CFD results, we are able to calculate the kinetic energy correction factors in the Bernoulli equation, and these estimated kinetic energy correction factors are used to calculate $\Delta P_{2,\text{est}}$ and $\Delta P_{3,\text{est}}$ of the experimental results.

The values of the $\Delta P_{2,\text{est}}$, $\Delta P_{3,\text{est}}$ and other important fluidic conditions for the estimation are listed in Table 5. The pressure drop results from the CFD simulations are within the uncertainty of the experimental pressure drop results (Figs. 8(*a*) and 8(*b*)). Since the flow regime of interest in this paper is single-phase, the ΔP_{total} only changes less than 4% before it changes to two-phase (Fig. 8(*b*)). Finally, the size of uncertainty bars in $\Delta P_{2,\text{est}}$, and $\Delta P_{3,\text{est}}$ increases as the flow rate increases. The details regarding calculation of $\Delta P_{2,\text{est}}$, and $\Delta P_{3,\text{est}}$ and their uncertainties are described in Appendix A2.

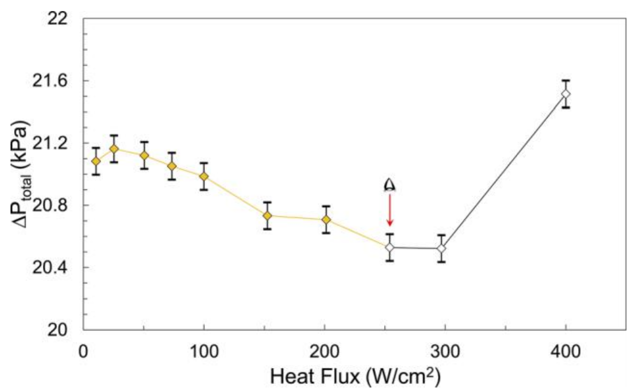

Fig. 9 Total pressure drop versus supplied heat flux. The void markers indicate that the flow regime is changed to two-phase. Inlet pressure is between 254 and 283 kPa.

Figure 9 shows the change of measured total pressure drop at the flow rate of 0.3 L/min. As the supplied heat increases, the total pressure drop slowly decreases because the dynamic viscosity of the coolant decreases with the increased fluid temperature. After the onset of nucleate boiling is visually observed at the heat flux of 254.0 W/cm^2, the gradual decrease in the total pressure drop is levels off and ΔP_{total} starts to increase as the heat flux increases. As the heat flux increases after the ONB event, the amount of generated vapor keeps increasing and this phenomenon leads to the drastic increase in the total pressure drop.

5 Conclusions

In this paper, we reported experimental results for the thermofluidic performance of the embedded microchannel-3D manifold cooler using R-245fa as the working fluid. The EMMC is capable of removing up to 300 W/cm^2 with pressure drop ~28.7 kPa, total thermal resistance of ~0.15 cm^2-K/W using single-phase R-245fa at the flow rate 0.37 L/min. The average HTC at the highest heat flux is ~50,000 W/m^2-K. As the fluid flow rate increases, the total thermal resistance is reduced due to improved convective heat transfer rate and reduced advection thermal resistance, while the conduction thermal resistance remains constant because it is limited by substrate's thickness and thermal conductivity.

The R_{total} at a given flow rate increases as the supplied heat flux increases, which is somewhat counterintuitive and unexpected. The uncertainty bars for the 25 W/cm^2 are large because the error associated with the temperature difference between the inlet fluid and average chip temperature (~3–5 °C). At higher heat fluxes 50–200 W/cm^2, the thermal resistance data are closer and small differences can be partially attributed to the temperature-dependent thermophysical properties of R-245fa. In general, CFD modeling at low heat fluxes and flow rates is recommended due to large uncertainty in the experimental results. There seems to be a systematic error in calculation of the net heat transferred to the fluid, q_{trans}, at the lowest heat flux of 25 W/cm^2.

The experimentally measured pressure drop results are compared with the conjugate CFD simulation results. The pressure drop results show the general changing trends: (i) the total pressure drop increases with the increased flow rate and (ii) the total pressure drop decreases as the supplied heat flux increases due to reduction in the dynamic viscosity of the coolant. Despite we do not have any visual access inside of the EMMC, the pressure drop in different zones of the EMMC can be estimated by the Bernoulli equation. The kinetic energy correction factors from the CFD simulation results are implemented to the Bernoulli equation to estimate experimental pressure drop in each EMMC zone. After all, the pressure drop results from the CFD simulations that are within the uncertainty of the pressure drop results from the experiments.

The 3D-manifold heat sink design makes access to the inlet and outlet plenum with thermocouples extremely difficult for measuring the inlet and outlet temperatures. As a result, the thermocouples are located at some distance away and susceptible to error associated with the heat loss from the fluid at the exit and heat gain at the entrance. Therefore, it is expected to see larger (and possibly systematic) error in calculation of q_{trans}, at the low heat fluxes. We have decided to share the thermal resistance results in order to demonstrate low fidelity results to be expected at low heat fluxes. In order to improve the accuracy of the inlet and outlet fluid temperature, we recommend IR thermometry at the inlet and outlet plenum regions from the cold-plate/heater side.

Acknowledgment

This project is supported by TOYOTA Research Institute of North America and the National Science Foundation Engineering Research Center for Power Optimization of Electro-Thermal Systems (POETS) with cooperative agreement EEC-1449548. The test structures were fabricated at the Stanford Nanofabrication Facility (SNF), and part of this work was performed at the Stanford Nano-Shared Facilities (SNSF).

Nomenclature

C_p = saturated specific heat (J/(kg-K))
g = gravitational acceleration (m/s^2)
h = head loss in microchannel (m)
H = height of microchannel (μm)
HTC = heat transfer coefficient (W/(m^2-K))
k = thermal conductivity (W/(m-K))
K_{gc} = coefficient of gradual contraction resistance
I = current (A)
L = length of microchannel (μm)
$\dot{m}$ = mass flow rate (kg/s)
N_{cp} = number of microchannels in CP
n = number of temperature intervals between $T_{\text{f,in}}$ and $T_{\text{f,out}}$
P = pressure (kPa)
Q = volume flow rate (L/min)
q_{heater} = supplied heat through the heater (W)
q_{loss} = heat loss during the heat transfer (W)
q_{trans} = transferred heat to increase sensible heat of the coolant (W)
q'' = heat flux (W/cm^2)
R = thermal resistance ((cm^2-K)/W)
Re = Reynolds number
$T_{\text{cp,base,avg}}$ = average temperature of microchannel base in CP (°C)
$T_{\text{heater,avg}}$ = average heater surface temperature (°C)
$T_{\text{heater,max}}$ = maximum heater surface temperature (°C)
U = uncertainty
v = fluid velocity (m/s)
V = voltage (V)
W = width of microchannel or fin(μm)
Z_{heater} = electric resistance of heater (Ω)
Z_0 = electric resistance of heater at room temperature (Ω)

Greek Symbols

α = temperature coefficient of resistance
γ = kinetic energy correction factor
δ_T = minute temperature interval to calculate sensible heat of fluid (°C)
Δ = difference
η_{fin} = individual fin efficiency
η_0 = overall fin efficiency
θ = angle (deg)
ρ = fluid density (kg/m^3)
ϕ = contribution of ΔP_2 and ΔP_3 to ΔP_{total}

Subscripts

adv = advection
cond = conduction
conv = convection
cp = cold-plate microchannel
est = estimation
f = fluid
fin = fin between cold-plate microchannels
gap = spacing between adjacent features
gc = gradual contraction
out = outlet
sat = saturated

Appendix

A.1 Determination of Single-Phase Flow Condition by Onset of Nucleate Boiling Correlation. We have calculated the onset of nucleate boiling at each test condition by using the ONB correlation from Ref. [14]. The shift in the inlet pressure with the changed flow rate is taken into account for the estimation. The estimated ONB points show good agreement with the visual inspection points in Fig. 10. The uncertainty bar size is mainly attributed to the uncertainty of average heated surface temperature. The measured maximum surface temperature is not used in the ONB estimation because they are local hotspots at the center and the heat is spread through thick Si bulk layer, 425 μm, that has isometric thermal conductivity of 130 W/m-K. The estimation matches well with the visually inspected ONB points.

A.2 Estimation of Pressure Drop and Its Uncertainty in the Embedded Microchannel-3D Manifold Coolers. Jung et al. [9] used a conjugate CFD simulation tool to predict the fluid pattern inside the test system, and they reported that the experimental results agreed well with the CFD simulation results within the allowable uncertainty of the pressure drop. If we assume that the working fluid is uniformly distributed across the manifold inlet

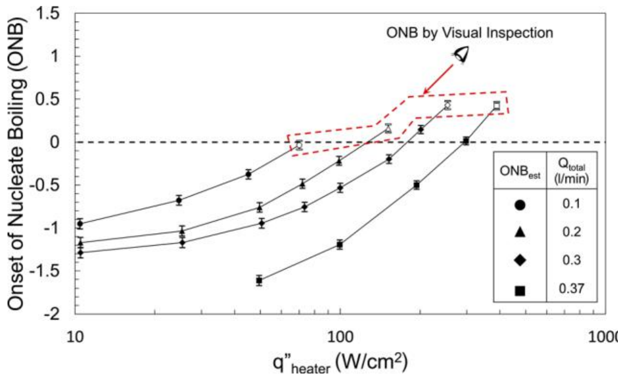

Fig. 10 Estimation of onset-of-nucleate boiling points for each test case, ONB estimation versus supplied heat flux at given flow rates. The dashed line indicates the threshold for ONB by the correlation [14] and the open markers designate the empirically captured ONB moments.

conduits, we can calculate the fluid velocity at the beginning and end of the gradual contraction region, v_1, and v_2, respectively (Table 5),

$$\frac{P_1}{\rho_{in} g} + \gamma \cdot \frac{v_1^2}{2g} = \frac{P_2}{\rho_{in} g} + \gamma \cdot \frac{v_2^2}{2g} + h_{gc}, \quad h_{gc} = K_{gc} \cdot \frac{v_2^2}{2g} \tag{A1}$$

$$\Delta P_{2,est} = P_1 - P_2 = \gamma \cdot \frac{\rho_{in}\left(v_2^2 - v_1^2\right)}{2} + \rho_{in} g \cdot h_{gc} \tag{A2}$$

$$\Delta P_{3,est} \cong \phi \cdot \Delta P_{total} - \Delta P_2, \quad \phi = 0.95 \tag{A3}$$

where ρ_{in} is the fluid density at the inlet fluid temperature, γ is the kinetic energy correction factor, 1.15–1.22, h_{gc} is the hydraulic head loss due to the gradual contraction, K_{gc} is the coefficient of gradual contraction resistance, 5.5×10^{-2} [15], v_1, P_1, are the fluid velocity and pressure at the beginning of the gradual contraction region, v_2, P_2 are the fluid velocity and pressure at beginning of the active cooling region. ϕ is introduced in Eq. (A3), representing the contribution of $\Delta P_{2,est}$ and $\Delta P_{3,est}$ to $\Delta P_{total,}$ which is assumed as 95%. The kinetic energy correction factor, γ, is 2 if the flow is fully developed, and laminar. If the flow is fully developed, and turbulent, γ is close to 1 [16]. By utilizing Eqs. (A1)–(A3), we can roughly estimate the pressure drop within the gradual contraction regions, $\Delta P_{2,est}$, and the pressure drop within the active cooling region, $\Delta P_{3,est}$ (Fig. 8). In Fig. 8, $\Delta P_{2,est}$ changes linearly, but $\Delta P_{3,est}$ parabolically changes as the flow rate increases. The estimated fluid velocities, the Reynolds numbers, and the pressure drop information are given in Table 5

$$(U_{\Delta P_{2,est}})^2 = \rho_{in}^2 \cdot \begin{bmatrix} (\gamma \cdot v_1 \cdot U_{v_1})^2 + \left\{(\gamma + K_{gc}) \cdot v_2 \cdot U_{v_2}\right\}^2 \\ +\left(\frac{v_2^2}{2} \cdot U_{K_{gc}}\right)^2 + \left(\frac{v_2^2 - v_1^2}{2} \cdot U_\gamma\right)^2 \end{bmatrix} \tag{A4}$$

$$(U_{\Delta P_{3,est}})^2 = \begin{bmatrix} (\Delta P_{total} \cdot U_\phi)^2 \\ +(\phi \cdot U_{\Delta P_{total}})^2 + \left(U_{\Delta P_{2,est}}\right)^2 \end{bmatrix} \tag{A5}$$

where the sources of the uncertainty calculation in Eqs. (A4) and (A5) are given in Table 6.

A.3 Detailed Description of Uncertainties.

As q_{heater} is calculated by two measured values, ΔV_{heater}, and I_{heater}, in Eq. (1), the measurement error is considered to calculate the uncertainty of q_{heater}

$$(U_{q_{heater}})^2 = \begin{bmatrix} (I_{heater} \cdot U_{\Delta V_{heater}})^2 \\ +(\Delta V_{heater} \cdot U_{I_{heater}})^2 \end{bmatrix} \tag{A6}$$

the measurement errors, $(U_{\Delta V_{heater}}/\Delta V_{heater}), (U_{I_{heater}}/I_{heater})$, are $\pm 0.1\%$ and the uncertainty of q_{heater} is calculated to be $\pm 0.14\%$. The uncertainty of the transferred heat, q_{trans}, is sum of the uncertainty of $dq_{trans,i}$

$$(U_{dq_{trans,i}})^2 = \left(\dot{m} \cdot \frac{C_{p,i} + C_{p,i+1}}{2}\right)^2 \cdot \begin{bmatrix} \left(\delta_T \cdot \frac{U_{\dot{m}}}{\dot{m}}\right)^2 + \left(\frac{U_{T_{f,in}}}{n}\right)^2 \\ +\left(\frac{U_{T_{f,out}}}{n}\right)^2 + \left(\delta_T \cdot \frac{U_n}{n}\right)^2 \end{bmatrix} \tag{A7}$$

$$U_{q_{trans}} = \sqrt{\sum_{i=1}^{n} \left(U_{dq_{trans,i}}\right)^2} \tag{A8}$$

the uncertainty of the saturated specific heat of the fluid is not considered in Eqs. (A7) and (A8). As noted, the uncertainty of $dq_{trans,i}$ is proportional to mass flow rate in Eq. (A7).

The uncertainties of $T_{heater,avg}$, Z_{heater} are given by

$$(U_{T_{heater,avg}})^2 = \begin{bmatrix} (U_{T_0})^2 + \left(\frac{Z_{heater}}{\alpha \cdot Z_0} \cdot \frac{U_{Z_0}}{Z_0}\right)^2 \\ +\left(\frac{U_{Z_{heater}}}{\alpha \cdot Z_0}\right)^2 + \left(\frac{Z_{heater} - Z_0}{\alpha \cdot Z_0} \cdot \frac{U_\alpha}{\alpha}\right)^2 \end{bmatrix} \tag{A9}$$

$$(U_{Z_{heater}})^2 = \left(\frac{U_{\Delta V_{heater}}}{I_{heater}}\right)^2 + \left(Z_{heater} \cdot \frac{U_{I_{heater}}}{I_{heater}}\right)^2 \tag{A10}$$

Based on Eq. (A9) and Table 5, the error in $T_{heater,avg}$ is less than 0.8 °C.

Table 6 Sources to estimate the uncertainties of $\Delta P_{2,est}$, $\Delta P_{3,est}$

Components	Affected parameters	Accuracy
Kinetic energy correction factor, γ	$\Delta P_{2,est}$	$\pm 5\%$
Gradual contraction resistance coefficient, K_{gc}	$\Delta P_{2,est}$	$\pm 5\%$
Proportion of $(\Delta P_2 + \Delta P_3)$ to ΔP_{total}, ϕ	$\Delta P_{3,est}$	$\pm 5\%$
Fluid velocities, v_1, v_2	$\Delta P_{2,est}$, $\Delta P_{3,est}$	$\pm 5\%$

Table 7 Thermofluidic and solver conditions for mesh independence study

Parameter	Unit	Value
Supplied heat flux	W/m^2	4.464×10^6
Mass flow rate	kg/s	8.263×10^{-3}
Inlet temperature	K	2.981×10^2
Solver model	–	SST *k*-omega (turbulent)

The uncertainties of R_{total} and R_{conv} are expressed as

$$(U_{R_{\text{total}}})^2 = \left[\left(\frac{U_{T_{\text{heater,avg}}}}{q''_{\text{trans}}}\right)^2 + \left(\frac{U_{T_{\text{f,in}}}}{q''_{\text{trans}}}\right)^2 + \left(R_{\text{total}} \cdot \frac{U_{q''_{\text{trans}}}}{q''_{\text{trans}}}\right)^2 \right] \quad \text{(A11)}$$

$$(U_{R_{\text{conv}}})^2 = \left[\left(\frac{U_{T_{\text{cp,base,avg}}}}{q''_{\text{trans}}}\right)^2 + \left(\frac{U_{T_{\text{f,ref}}}}{q''_{\text{trans}}}\right)^2 + \left(R_{\text{conv}} \cdot \frac{U_{q''_{\text{trans}}}}{q''_{\text{trans}}}\right)^2 \right] \quad \text{(A12)}$$

As the supplied heat flux increases, the size of denominators on the right side of Eqs. (A11) and (A12) increases. As a result, the uncertainty of R_{total} and R_{conv} decrease with the increased heat flux.

The uncertainty of HTC is given by

$$\left(\frac{U_{\text{HTC}}}{\text{HTC}}\right)^2 = \left[\left(\frac{U_{q_{\text{trans}}}}{q_{\text{trans}}}\right)^2 + \left(\frac{U_{A_{\text{wet}}}}{A_{\text{wet}}}\right)^2 + \left(\frac{U_{T_{\text{cp,base,avg}}}}{T_{\text{cp,base,avg}} - T_{\text{f,ref}}}\right)^2 + \left(\frac{U_{T_{\text{f,ref}}}}{T_{\text{cp,base,avg}} - T_{\text{f,ref}}}\right)^2 \right] \quad \text{(A13)}$$

With a constant heat flux condition, $T_{\text{f,ref}}$ in the denominator of the third and fourth terms in Eq. (A13) is constant and $T_{\text{cp,base,avg}}$ decreases as the flow rate increases. Therefore, $T_{\text{cp,base,avg}} - T_{\text{f,ref}}$ should decrease as the flow increases at a constant heat flux. As a result, the size of HTC uncertainty bar increases as the flow rate increases. In addition, the size of HTC uncertainty bar also increases as the supplied heat flux decreases. The uncertainty of q_{trans} calculated by Eqs. (A7) and (A8) is a function of n, which is the number of intervals between $T_{\text{f,out}}$ and $T_{\text{f,in}}$. The n is reduced as the heat flux decreases because the size of temperature interval is fixed but $T_{\text{f,out}} - T_{\text{f,in}}$ decreases. In Eq. (A7), the (U_n/n) is one of the terms to attribute to the uncertainty of $dq_{\text{trans,i}}$; therefore, the reduced n leads to the increased uncertainty of $dq_{\text{trans,i}}$.

A.4 Mesh Independence Study of Conjugate Computational Fluid Dynamics Simulations. The experimental results are validated by conjugate numerical simulations, ANSYS FLUENT 18.1 (Canonsburg, PA), for the exact EMMC geometry (Table 1). The thermofluidic and the solver conditions for the mesh independence study are listed in Table 7.

The number of mesh elements varies from 5 to 32×10^6, and the results are plotted in Fig. 11. There are less than 0.6% change in the average and maximum heater temperature, and the total pressure drop if the number of mesh elements is more than 25×10^6. In addition, the experimentally measured temperature and pressure drop values are superimposed in Fig. 11 and the CFD simulation results are well matched to the experimental results. Therefore, we have used 25×10^6 of mesh elements in this study.

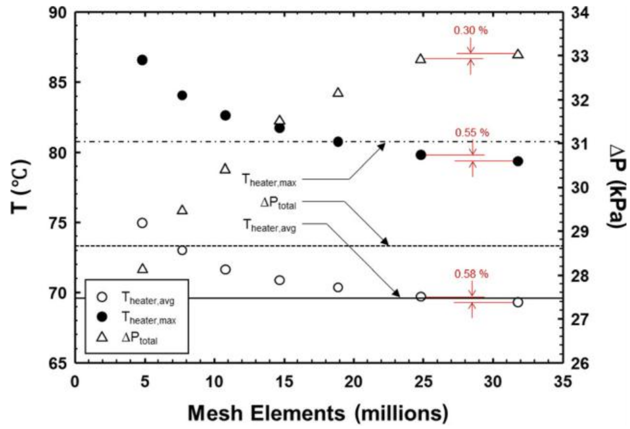

Fig. 11 Summarized heater temperatures and pressure drop results for the mesh independence study. The results are plotted as a function of the mesh elements. The results with more than 25×10^6 of mesh elements show good simulation convergence, <0.6%.

References

[1] Tuckerman, D. B., and Pease, R. F. W., 1981, "High-Performance Heat Sinking for VLSI," IEEE Electron Dev. Lett., **2**(5), pp. 126–129.
[2] Drummond, K. P., Weibel, J. A., Garimella, S. V., Back, D., Janes, D. B., Sinanis, M. D., and Peroulis, D., 2016, "Evaporative Intrachip Hotspot Cooling With a Hierarchical Manifold Microchannel Heat Sink Array," Intersociety Conference on Thermal and Thermomechanical Phenomena in Electronic Systems (ITherm), Las Vegas, NV, May 31–June 3, pp. 307–315.
[3] Drummond, K. P., Back, D., Sinanis, M. D., Janes, D. B., Peroulis, D., Weibel, J. A., and Garimella, S. V., 2018, "Characterization of Hierarchical Manifold Microchannel Heat Sink Arrays Under Simultaneous Background and Hotspot Heating Conditions," Int. J. Heat Mass Transfer, **126**, pp. 1289–1301.
[4] Cetegen, E., 2010, *Force Fed Microchannel High Heat Flux Cooling Utilizing Microgrooved Surfaces*, Ph.D. University of Maryland, College Park, MD.
[5] Goodson, K. E., Chen, C. H., Huber, D. E., Jiang, L., Kenny, T. W., Koo, J.-M., Laser, D. J., Mikkelsen, J. C., Santiago, J. G., Wang, E. N.-Y., Zeng, S., and Zhang, L., 2005, "Electroosmotic Microchannel Cooling System," US Patent No. 6,942,018.
[6] Goodson, K. E., Kenny, T. W., Zhou, P., Upadhya, G., Munch, M., McMaster, M., and Hom, J., 2006, "Method and Apparatus for Achieving Temperature Uniformity and Hot Spot Cooling in a Heat Producing Device," US Patent No. 7,104,312.
[7] Jung, K. W., Harza, S., Kwon, H., Piazza, A., Jih, E., Asheghi, M., Gupta, M. P., Degner, M., and Goodson, K. E., 2019, "Design Optimization of Silicon-Based Embedded Microchannels and 3D-Manifold for High Heat Flux (>1 kW/cm^2) Power Electronics Cooling," ASME Paper No. IPACK2019-6400.
[8] Zhou, F., Joshi, S. N., Liu, Y., and Dede, E. M., 2019, "Near-Junction Cooling for Next-Generation Power Electronics," Int. Commun. Heat Mass, **108**, p. 104300.
[9] Jung, K. W., Kharangate, C. R., Lee, H., Palko, J., Zhou, F., Asheghi, M., Dede, E. M., and Goodson, K. E., 2019, "Embedded Cooling With 3D Manifold for Vehicle Power Electronics Applications: Single-Phase Thermal-Fluid Performance," Int. J. Heat Mass Transfer, **130**, pp. 1108–1119.
[10] Incropera, F. P., 2011, *Fundamentals of Heat and Mass Transfer*, Wiley, Hoboken, NJ.
[11] Jung, K. W., Hazra, S., Kwon, H., Piazza, A., Jih, E., Asheghi, M., Gupta, M. P., Degner, M., and Goodson, K. E., 2020, "Thermal and Manufacturing Design Considerations for Silicon-Based Embedded Microchannel-3D Manifold Coolers (EMMCs)—Part 2: Parametric Study of EMMCs for High Heat Flux (~1 kW/cm^2) Power Electronics Cooling," ASME J. Electron. Packag., Epub.
[12] Hazra, S., Jung, K. W., Iyengar, M., Malone, C., Asheghi, M., and Goodson, K. E., 2020, "Thermal and Manufacturing Design Considerations for Silicon-Based Embedded Microchannel-3D Manifold Coolers (EMMCs)—Part 3: Addressing Challenges in Laser Micro-Machining Based Manufacturing of 3D-Manifolded Micro-Cooler Devices," ASME J. Electron. Packag., Epub.
[13] Belser, R. B., and Hicklin, W. H., 1959, "Temperature Coefficients of Resistance of Metallic Films in the Temperature Range 25 to 600 C," J. Appl. Phys., **30**(3), pp. 313–322.
[14] Liu, D., Lee, P.-S., and Garimella, S. V., 2005, "Prediction of the Onset of Nucleate Boiling in Microchannel Flow," Int. J. Heat Mass Transfer, **48**(25–26), pp. 5134–5149.
[15] Mott, R. L., and Untener, J. A., 2014, *Applied Fluid Mechanics*, 7th ed., Pearson Education, New York.
[16] Cengel, Y. A., and Cimbala, J. H., 2006, *Fluid Mechanics*, McGraw-Hill, New York.